Toward the Digital Twin of Additive Manufacturing – Integrating Thermal Simulations, Sensing, and Analytics to Detect Process Faults

Aniruddha Gaikwad, Reza Yavari, Mohammad Montazeri,
Kevin Cole, Linkan Bian, and Prahalada Rao.

Abstract

The goal of this work is to achieve the defect-free production of parts made using additive manufacturing (AM) processes. As a step towards this goal, the objective is to detect flaws in AM parts during the process by combining predictions from a physical model (simulation) with in-situ sensor signatures in a machine learning framework. We hypothesize that flaws in AM parts are detected with significantly higher statistical fidelity (F-score) when both in-situ sensor data and theoretical predictions are pooled together in a machine learning model, compared to an approach that is based exclusively on machine learning of sensor data (black-box model) or physics-based predictions (white-box model). We test the hypothesized efficacy of such a *grey-box* model or *digital twin* approach in the context of the laser powder bed fusion (LPBF) and directed energy deposition (DED) AM processes. For example, in the DED process, we first predicted the instantaneous spatiotemporal distribution of temperature in a thin-wall titanium alloy part using a computational heat transfer model based on graph theory. Subsequently, we combined the preceding physics-derived thermal trends with in-situ temperature measurements obtained from a pyrometer in a readily implemented supervised machine learning framework (support vector machine). We demonstrate that the integration of temperature predictions from an *ab initio* heat transfer model and in-situ sensor data is capable of detecting flaws in the DED-produced thin-wall part with F-score approaching 90%. By contrast, the F-score decreases to nearly 80% when either temperature measurements from the in-situ sensor or temperature distribution predictions from the theoretical model are used alone by themselves. This work thus demonstrates an early foray into the digital twin paradigm for real-time process monitoring in AM via seamless integration of physics-based modeling (simulation), in-situ sensing, and data analytics (machine learning).

Key Words: Additive Manufacturing, Digital Twin, Thermal Simulations, Graph Theory, Data Analytics, Machine Learning, Sensors, Laser Powder Bed Fusion, Directed Energy Deposition, Thermal Camera, Photodetector, Pyrometer.

1 Introduction

1.1 Overview and Objective

The goal of this work is to ensure the defect-free production of parts made using additive manufacturing (AM) processes. The design and manufacturing flexibility offered by AM is valuable in a variety of strategic applications ranging from aerospace to biomedical [1]. For instance, using AM to make parts for the Cessna Denali aircraft engine decreased the number of components from 855 to 12, and increased the fuel efficiency of the engine, as well as its power by over 10 percent [2]. However, industries such as aerospace are hesitant to use AM-produced parts for mission-critical components due to the existing lack of process consistency and significant variation in physical properties between parts [3, 4].

This work concerns two specific AM processes used for making metal parts, namely, directed energy deposition (DED) and laser powder bed fusion (LPBF) [3]. In both LPBF and DED, metal in the form of powder is fused (melted) layer-upon-layer using a high-energy laser. The instantaneous spatiotemporal distribution of temperature in the part during the printing process governs the formation of defects, e.g., porosity and distortion in part shape [5, 6].

As a step toward the goal of defect-free AM, the objective of this work is to detect incipient faults in LPBF and DED processes. To realize this objective, we use a two-step approach. First we predict the temperature distribution in the part with a novel graph theory-based computational heat transfer approach [7]. Subsequently, we combine the theoretically-predicted temperature distribution with thermal signatures acquired using in-situ sensors during the printing process in a machine learning model, which is trained to detect process faults, such as porosity (supervised learning).

To provide an analogy, the theoretical model is a simulacrum – a *digital twin* – of the actual AM process, whose status is continually updated with in-situ real-time sensor data observations so that potentially deleterious process excursions are detected and corrected in real-time [8-10].

The central hypothesis of this paper is that such a or *digital twin* approach *or grey-box* model that combines the theoretical temperature predictions with in-situ sensor data leads to higher statistical fidelity of fault prediction in comparison to models that are based exclusively on either theoretical predictions or sensor-related information alone [11, 12]. We test the foregoing hypothesis in the context of two practical AM case studies; one from LPBF and another from DED [5, 6].

1.2 Rationale and Significance

The concept of the digital twin is exemplified in Figure 1. The digital twin approach or grey-box modeling combines the advantages of physics-based models (white-box) and data-driven models (black-box). White-box models typically consist of deterministic equations that encapsulate the physics of a process. For instance, the spatiotemporal distribution of temperature in an AM part is captured in terms of the heat equation, which is a second-order partial differential equation (described later in Sec. 3). While physical models are essential to understand the causal process phenomena, they are ill-suited to capture stochasticity (uncertainty), and the computational burden increases with inclusion of multi-scale phenomena [14, 18, 19].

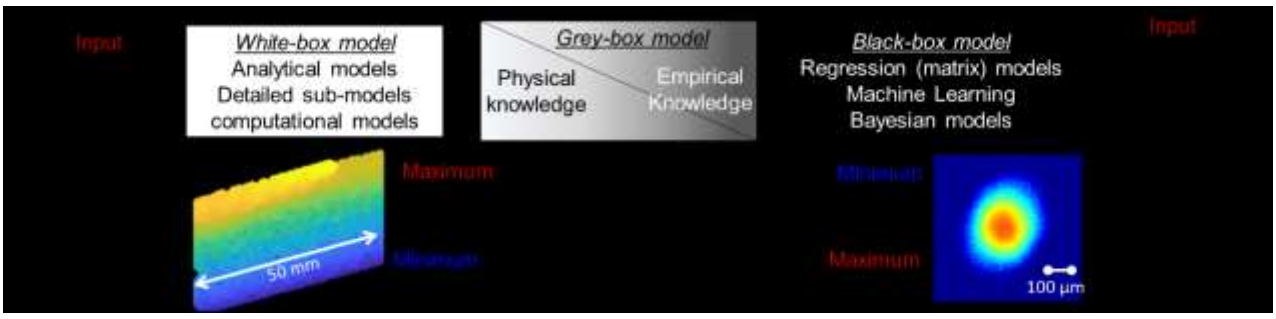

Figure 1: The concept of the digital twin (gray box modeling) approach in the context of the DED AM process.

In contrast, black-box models are constructed from empirical data alone; they relate process signatures extracted from sensors to observations. While data-driven models are adept at accommodating the uncertainty (variation) in the physical processes, their ability to interpret and explain the phenomena at the root of a flaw is inferior in comparison to white-box models [11, 12]. The interpretability limitation of data-driven models also constrains their use for process correction, as there is no theoretical guideline to bring the process back to its fault-free status once an anomaly is detected.

The digital twin approach can significantly impact AM in the following three ways [8-10]:

(i) optimize the process parameters, such as laser power and scan speed, and provide guidelines for part design, build orientation and placement of supports based on process physics as opposed to expensive empirical testing;

(ii) serve as a basis for detection and monitoring of incipient process faults by combining theoretical predictions with real-time sensor data, and thereby provide a basis for model-based feedforward control in AM. We note that faults could include those inherent to the process, as well as those introduced through malicious cyber-physical intrusions; and

(iii) reduce the computational burden involved in multi-scale modeling, as well as storing and analyzing a large volume of in-situ sensor data.

1.3 Novel Contribution

The unique contribution of this work is in augmenting real-time in-situ sensor data obtained at the laser-material interaction zone, called the meltpool (100 μm scale), with theoretically-derived part-level temperature distribution (millimeter scale) to monitor the LPBF and DED processes (see Figure 1, in Sec. 2.1).

This work overcomes one of the main challenges in realizing the digital twin for AM, viz., the computational burden involved in obtaining the part-level thermal distribution. It currently takes several hours, if not days, for non-proprietary mesh-based finite element (FE) models to predict the temperature distribution inside an AM part as it is being printed [13-15].

While commercial solutions, such as Autodesk's Netfabb, have reduced the computation time through adaptive meshing-based FE techniques, the underlying mathematics remain proprietary and are therefore not tractable for integrating in-situ sensor data [13]. This work reduces the challenge of computational burden in simulating the thermal profile in AM parts by applying a recently published graph-theoretic computational heat transfer approach [7]. This approach was shown to predict the temperature distribution in AM parts within 10% of the time required by FE analysis and with error less than 10% [7].

However, the graph theory approach remains to be tested and applied to a practical AM data set. This paper applies the graph-theoretic heat transfer model for the first time to real-world AM data and demonstrates its effectiveness from a process monitoring viewpoint by integrating the model predictions with in-situ sensor data.

In closing this section, we note that this paper uses in-situ sensor data described in the authors' prior publications [16, 17]. However, these previous publications were focused exclusively on data-driven machine learning approaches for process monitoring and defect detection. None of these prior publications combined sensor data and thermal modeling. In the same vein, concerning the graph-theoretic thermal model published in Ref. [7], the approach has not yet been applied to any of the data sets described in Ref [16, 17].

1.4 Organization of the paper

The rest of this paper is organized as follows. The rationale for the digital twin, along with a review of the prior work, is provided in Section 2. The graph-theoretic approach for modeling the temperature distribution in metal AM processes is explained in Section 3. Next, in Section 4 and Section 5 the efficacy of the digital twin approach to detect process flaws is demonstrated via case studies from the LPBF and DED metal AM processes, respectively. Finally, conclusions and avenues for future work are given in Section 6.

2 Literature Review

The burgeoning need for a digital twin strategy to overcome the process repeatability and part quality challenges in AM is motivated in the pioneering works of DebRoy *et al.* and Yang, who provided an overarching framework for its implementation and demonstrated its efficacy via practical case studies [8-12]. We note that DebRoy *et al.* [8-10] refer to the approach as the *digital twin for AM,* while *grey-box modeling* is a term used by Yang *et al.* [11, 12].

This section has two parts; the first, Sec. 2.1, discusses the need for the digital twin in AM; the second part, Sec. 2.2, reviews the pioneering work in the area.

2.1 Need for a Digital Twin Approach in AM.

Achieving the digital twin is valuable in AM in the following three ways [8-10].

1) Physics-based optimization of the AM process

The process parameters and part features in metal AM are currently finalized through empirical design of experiments-based optimization [20]. There are two drawbacks with a purely empirical approach. First, the vast part design, material and process parameter space in metal AM processes, such as LPBF and DED is compounded by the relatively expensive process consumables, slow speed, and the small batch size of parts produced [9].

Second, the process parameters optimized for one type of part design may not yield optimal results when used with a different part design even with the same material. This is because the microstructure evolved and mechanical properties are dependent on the spatiotemporal heat distribution in the part as it is printed, which in turn is a function of the shape (geometry) of the part, part orientation, scan strategy, support structures, layout of the build, among others [14]. Hence, an empirical *build-and-test* optimization strategy is prohibitively expensive and time-consuming in AM, and provides no assurance that the part will have the desired properties [8]. The digital twin approach provides a route to transition AM from the current status quo of empirical optimization to physics-based optimization.

2) Real-time monitoring and model-based feedforward control of the process

Process monitoring in AM can be viewed within the context of both faults intrinsic to the process, as well as malicious intrusions. At present process monitoring in AM is primarily based on analysis of in-situ sensor data, which are subsequently linked to part flaws, part geometries and process conditions using machine learning models [21, 22].

For instance, machine learning techniques, such as neural networks are trained from previous data (supervised learning) to recognize patterns, such as melt pool shape and size, and these patterns are correlated with defect characteristics based on offline characterization of the part quality, such as using X-ray Computed Tomography (XCT) to stratify the severity and location of defects; XCT is a tedious undertaking [23]. Unsupervised machine learning techniques, such as self-organizing maps, have also been pioneered recently to cluster signal patterns, but these too rely on offline XCT analysis for ground-truth verification [17].

The specific drawbacks of using purely data-driven approaches for monitoring of process faults in AM are as follows.

(i) A large amount of heterogeneous in-situ streaming sensor data, ranging from 1-dimensional temperature data to high-speed 2-dimensional video is often acquired. There is a ponderous computational burden involved with storage and analysis of such a high volume and variety of sensor data – a big data problem.

(ii) Each part geometry, part orientation, build plan, and process parameter set is linked to a unique signal pattern, implying that the data-driven models will have to be retrained if any of the process conditions change, and which further impedes the transferability of the data-driven model across different AM platforms.

(iii) The complex nature of machine learning techniques, such as deep learning, occludes interpretability of the causal physical mechanisms that cause defect formation [24-26];

(iv) The training process for supervised machine learning mandates comprehensive observational data sets representing different types of process scenarios and faults, which are expensive to obtain [25]. Furthermore, machine learning approaches often require the extraction of a relatively large number of input features from the sensor signatures, which adds to model complexity and is liable to cause prediction uncertainty.

(v) Data-driven approaches do not provide a physical basis to correct the process once a flaw has been detected.

3) Reducing the computational burden in modeling and data analytics

The defects in AM parts are caused by distinctive scale-dependent mass and heat transfer phenomena [14]. These phenomena range from the laser-material interaction zone, called the meltpool-level (< 100 μm) to the part-scale (1 mm and above). It is computationally tortuous to encapsulate such multi-scale phenomena within a physical model [14].

An alternative strategy, demonstrated in this work, is to augment the part-scale temperature distribution predicted from a theoretical model with finer meltpool-scale temperature trends observed using in-situ sensors. This exchange of complementary information between the theoretical model and sensor data not only reduces the computational burden concerning the theoretical model, but also limits the volume of sensor data that needs to be stored and analyzed.

2.2 Prior Work in the Digital Twin in AM.

We review the work of DebRoy *et al.* [8-10] in depth, given its contextual similarity with our own. These papers underscore the importance of seamless integration of physical process modeling, sensing, and analytics as a keystone of the digital twin concept.

To create a digital twin for AM from the process optimization and control perspective, Mukherjee and DebRoy suggest that there is a need for three crucial components: a mechanistic model, sensor data, and an interface between the mechanistic model and sensor data, which can take the form of a machine learning model [10]. The authors posit that the mechanistic model should be able to determine the optimum processing conditions within a reasonable amount of time. The in-situ sensors should then monitor the process for drifts and control of the process should be guided by the mechanistic model to obtain a part with near-ideal properties. Finally, the purpose of the machine learning interface is to compare the results between the mechanistic model and the post-build results (obtained from offline characterization techniques, such as XCT) to suggest changes in the physical model, part design, and processing.

DebRoy *et al.* assert that the digital twin cannot entirely supplant experimental studies, but will aid in reducing the number of experiments required to make AM parts with minimal defects [8]. To demonstrate the concept of the digital twin, DebRoy *et al.* present a novel framework of a mechanistic model to predict the meltpool-level phenomena such as solidification rates,

temperature gradients, cooling rates, velocity field, and as a consequence determine the microstructure and mechanical properties (hardness) of stainless steel 316L and Alloy 800H (iron-nickel-chromium alloy) parts made using DED process [8].

Two main differences can be distilled between our work and that of DebRoy *et al.* [8-10]. First, the work of DebRoy is focused on predicting the effect of meltpool-level phenomena and solidification rates on the microstructural evolution. In our work, the emphasis is on predicting the part-level thermal phenomena and its effect on defects, such as porosity and distortion. In other words, we predict the temperature distribution at the overall part-level where the thermal phenomena are in the scale of millimeters and beyond; the work of Debroy *et al.* predicts the meltpool-level phenomena which ranges from tens of micrometers to few hundred micrometers. Predicting the shape and solidification rates at the meltpool-level is contingent on thermal and fluid flow phenomena, while the part-level thermal model used in this work ignores the meltpool phenomena, such as latent heat losses [14, 18, 19].

The meltpool-level models are geared toward prediction of the microstructural evolution as a function of the process parameters. By contrast, prediction of the part-level thermal distribution is aimed at predicting large-scale effects, such relationship between the process parameters, part design, and build conditions (supports and orientation) on defects, such as porosity, distortion in the part geometry and thermal-induced stresses. To summarize, the prediction of meltpool intrinsically involves merging of both computational fluid dynamics and heat transfer aspects, while the prediction of the part-level thermal distribution involves computational heat transfer.

Second, and a key differentiator herein, is that we complement the theoretical prediction of the temperature distribution at the part-level with in-situ sensor data in a machine learning framework. Specifically, the digital twin is used in this work to monitor the build condition in the

LPBF and DED processes by merging the part-level thermal distribution predictions with in-situ sensor data, such as photodetectors and pyrometers that capture the meltpool-level phenomena. The near real-time nature of this digital twin is the first step towards a feedforward closed-loop control in AM. Finally, we note that physical modeling in AM is a mature and vast area, and is a multi-scale domain; the challenges and recent research in the area are reviewed in [13-15, 19, 27].

3 Thermal modeling using Graph Theory

The aim of part-level thermal modeling in AM is to solve the following continuum heat diffusion equation. Solving the heat diffusion results in the spatiotemporal temperature distribution $T(x, y, z, t)$ at every location (*x, y, z)* inside the body at time t.

$$\rho c_p \frac{\partial}{\partial t} T(x, y, z, t) - k \left(\frac{\partial^2}{\partial x^2} + \frac{\partial^2}{\partial y^2} + \frac{\partial^2}{\partial z^2} \right) T(x, y, z, t) = Q(x, y, z, t) \quad (1)$$

The material constants are, ρ the density of the part material; c_p specific heat; and *k* thermal conductivity. The right hand-side is the heat input Q at a location (*x, y, z)* at time *t*. In the context of the LPBF or DED , the heat input Q [J.m^{-3}] is the energy supplied by the laser.

The key concept in the heat equation is that a certain proportion of the heat supplied (Q) is used to increase the temperature of the body, represented by the first derivative term $\frac{\partial T(x,y,z,t)}{\partial t}$ on the left-hand side, and is contingent on its material properties. The rest of the heat supplied is lost to the surroundings governed by the shape of the part, and is captured by the second derivative term $\left(\frac{\partial^2}{\partial x^2} + \frac{\partial^2}{\partial y^2} + \frac{\partial^2}{\partial z^2} \right) T(x, y, z, t)$ called the continuous Laplacian operator $\boldsymbol{\Delta}$.

The graph-theoretic approach for solving the continuum heat equation is based on discretizing the continuous Laplacian operator $\boldsymbol{\Delta}$, by a weighted and undirected graph over a grid of points (nodes) sampled within the geometry of the part [7]. The continuous Laplacian operator $\boldsymbol{\Delta}$ is then

approximated by a discrete Laplacian operator (**L**) called the graph Laplacian matrix. As shown in our recently published work, the discrete heat equation is solved as a function of the eigenvectors (**ϕ**) and eigenvalues (**Λ**) of the Laplacian matrix. The solution takes the following form, with T_0 as the melting temperature of the material.

$$T(x, y, z, t) = \boldsymbol{\phi} e^{-\frac{k}{\rho c_p} g \boldsymbol{\Lambda} t} \boldsymbol{\phi}' T_0 \tag{2}$$

In the graph-theoretic solution, g is a model parameter added to reconcile the units and influence the rate of heat diffusion. The parameter g, called the gain factor, is calibrated offline for a specific type of material with experimental data and Green's function analysis [7]. We further consider that the boundaries of the part to lose heat as per Newton's law of convection.

The advantage of the graph-theoretic solution is that instead of solving the heat equation for each element through element birth-and-death techniques as in finite element (FE) analysis, we track the temperature distribution in the AM part in terms of nodes of a planar graph projected onto its geometry [7]. While the FE-based approach requires computationally intensive matrix inversion at each time step, the graph-theoretic method instead relies on parsimonious matrix multiplication for each time step [13, 15].

Our previous work shows that the time taken by the graph theory to predict the temperature distribution for a fixed error-level of 5% in reference to the exact analytical solution obtained using Green's function is about $1/10^{th}$ of the time required by FE analysis [7]. Computational benchmarking studies with AM test geometries also indicated that the graph theory approach results in a thermal distribution trend that is within 10% in the fraction of time required by the so-called Goldak's computational FE analysis model used in the AM literature [13, 15]. For instance, for a representative AM part the graph theory approach required less than 20 minutes to converge,

compared to over 3 hours with FE analysis, and the difference between the FE analysis and graph theory models was less than 10% [7].

4 Case 1 - Implementing the Digital Twin in Laser Powder Bed Fusion (LPBF)

4.1 Rationale

This section demonstrates the digital twin concept in the context of LPBF process. Many existing studies for the data-driven modeling of thermal history mainly focus on test artifacts with simple shapes [28]. However, due to the change of effective thermal conductivity, the data-driven features vary during the fabrication of parts with more complex geometries (e.g., overhang structure). To implement accurate design and *in-situ* monitoring of LPBF, it is critical to understand and capture the changes in data-driven features as a function of the local geometry. The aim is to establish the thermal-geometry relationship based on the in-situ data guided by *a priori* predictions from the graph theory model.

Accordingly, a part with a steep overhang geometry is built on a commercial LPBF platform (EOS M270) as shown in Figure 2. Overhang structures are challenging to build, and often fail to have desired properties [29, 30]. The main cause for the failure of parts with significant overhang geometries is the prevalence of high temperatures in the overhang region [31, 32]. This is because the area underneath the overhang feature, if unsupported, is composed of raw powder, which has poor thermal conductivity compared to a fully consolidated part. The high temperatures generated in the melting of the overhang features create aberrations in the meltpool leading to poor surface finish and microstructure heterogeneity [29, 32].

Understanding the dynamical nature of the thermal field in an overhang structure is critical for adjusting the baseline for design and process monitoring. By simulating the temperature distribution of the overhang before-hand, practitioners can anticipate potential regions for failures.

The theoretical simulation also serves as a reference benchmark for data-driven analysis, for instance, instead of tracking every location of the build with sensors, resulting in extremely large data sets, only certain critical locations, prone to failures such as near the vicinity of overhang features can be monitored more closely. Accordingly, using a theoretical model will reduce the volume of sensor data that must be stored, thus making defect detection more computationally tractable, but also provide a forward-looking tool to guide part design and build planning.

The developed graph-theory derived temperature trends are validated by benchmarking against the actual part geometry specified in the G-code. The exact location where the laser transitions from the bulk area of the part to the overhang region is precisely traceable from the design of the part and G-code implemented in the machine. This one-to-one matching of the laser position from the G-code, the temperature predicted from the graph theory model, and meltpool-level data collected by the sensors provides the baseline information to rigorously benchmark the results before the digital twin can be implemented for in-practice complex parts.

4.2 Experimental Setup and Data Acquisition Procedure

An overhang nickel alloy 625 (popularly called Inconel 625) structure consisting of 800 layers, as shown in Figure 2(a), was built using an EOS M270 LPBF machine at National Institute of Standards and Technology (NIST) [16]. The experimental details are described in Ref. [16]. An important aspect of the build that influences the thermal distribution in the part is the use of a stripe-wise scanning pattern. This laser scan strategy is described later in the context of Figure 4. To explain briefly, a stripe is a section of the part that is scanned by the laser in a meandering line-by-line pattern. Each line segment inside a stripe is called a hatch. Process signatures are acquired with a shortwave infrared (SWIR) thermal camera and a photodetector (Figure 2(b)). Close to 5 gigabytes of sensor data are obtained per layer.

Given challenges with storage of such as large amount of heterogeneous data, the thermal camera is active for a few layers; we have analyzed data from one layer in this work which is at a height of 7.9 mm as shown in Figure 2(b). The data acquired from these sensors display distinctive signatures while scanning the overhang and bulk (non-overhang) section of the part. For instance, in Figure 3 (b-d) it is evident from the thermal camera images that the meltpool in the overhang section is approximately 1.5 times in length as compared to the meltpool of the bulk section.

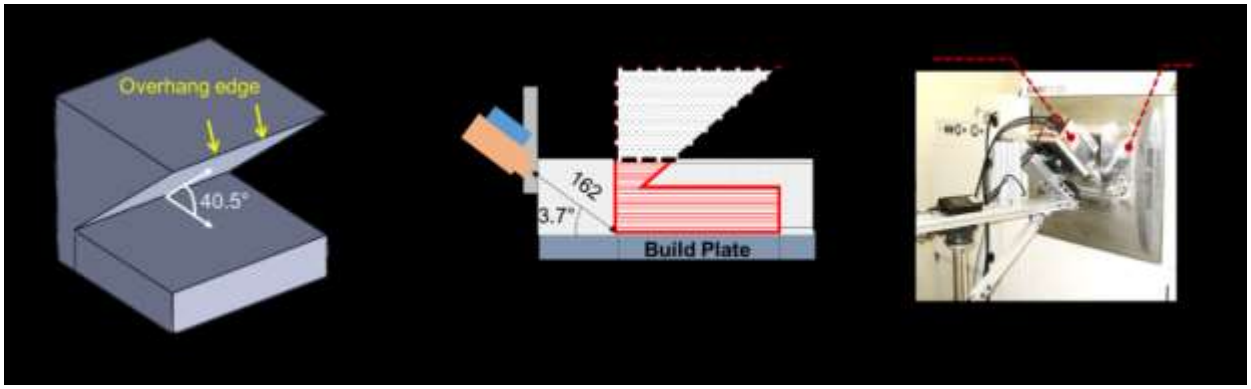

Figure 2: (a) 3-D schematic representation of the overhang part. (b) Schematic of the sensing setup with respect to the part. Sensor data from layer at height 7.9 mm is used in this work. (c) A photograph showing the location of the thermal camera with respect to the LPBF machine. (All dimensions are in mm).

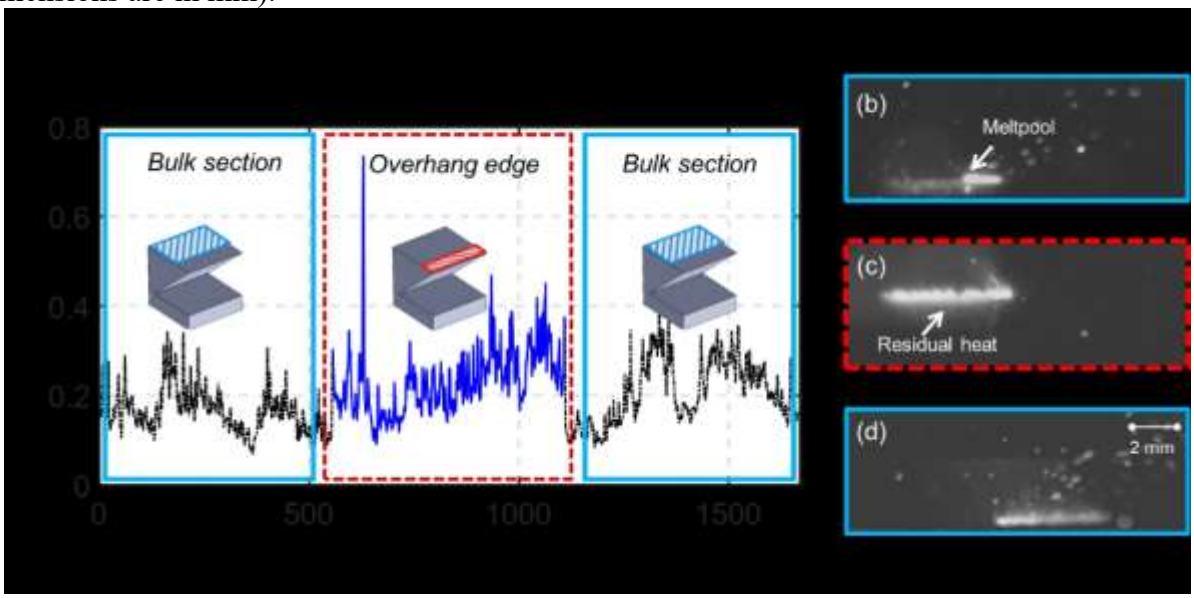

Figure 3: (a) Photodetector signal and the corresponding thermal camera frames (right) of bulk and overhang section. (b-d) Accumulation of residual heat is observed in the thermal camera frame of the overhang section.

This can be attributed to the residual heat in the overhang section. Similarly, the photodetector signals in Figure 3 (a) show a fleeting difference in the overhang and bulk section. To reiterate, in this work, we use the data collected from the photodetector to distinguish between the overhang and bulk section of the test artifact to demonstrate the digital twin concept. The G-code in the machine provides the location of the laser so that the sensor data is matched precisely to the laser position.

We note that there is an impetus to replace a high-fidelity sensor, such as a thermal camera, that requires intensive data storage and post-processing, with a low-fidelity and much less expensive sensing approach, such as a photodetector, which can also acquire data throughout the build process at sampling rates approaching 1 MHz. The thermal camera used in this work costs over three hundred thousand dollars, while a photodetector can be acquired for within $500. Thus, replacing a high-fidelity sensor such as thermal camera, with a low fidelity sensor yet inexpensive sensor will be advantageous practically. In this work, the thermal camera is used as a ground-truth against which the performance of the photodetector is assessed.

However, the photodetector data is a time series data which provides no spatial information to distinguish between the overhang and bulk section of the test artifact. The photodetector data is therefore synchronized with the thermal camera data to establish spatial correlation. One image of the thermal camera corresponds to 500 data points of the photodetector. Since one hatch of the laser consists of 10 thermal camera images, thus the photodetector data is divided into 10 windows of ~500 data points to demarcate a hatch.

We only used the data from stripe 2 and 3 (Figure 4) to demonstrate the concept and eliminate edge effects. We considered three of the hatches from each stripe near the edge to represent the

overhang feature as shown in Figure 4. Thus, 60 windows of the photodetector data belong to the overhang section. Statistical features, such as mean and standard deviation of each of these windows are calculated from the photodetector signal, and from the intensity readings of the thermal camera.

4.3 Thermal simulation of the LPBF test sample with overhang feature

The thermal simulation is discretized into 10 blocks per hatch with 4 nodes per block. The simulation parameters are derived based on the calibration procedures described in Ref. [7]. The overhang part is built by adopting the below-explained laser scanning regime.

1) Each layer of the part is built in a stripe-wise pattern as shown in Figure 4. The length of each stripe, (S_L) is set to be 4 mm, and there are four stripes per layer.
2) A raster pattern is employed to sinter each stripe. A single stripe is a hatch with thickness h_t (Figure 4). In this work, the hatch thickness is 0.1 mm.
3) Each hatch is sintered in a block-by-block fashion to resemble the LPBF process (Figure 5). The length of each block, b_L (Figure 4) is set to be 0.4 mm, and there are 10 blocks per hatch.

The simulation of the LPBF process for a layer at 7.9 mm height is represented in Figure 4. The layer is sintered in a stripe-wise pattern identical to the physical build. Further, each stripe is sintered hatch-by-hatch, and subsequently, each hatch is sintered block-by-block as shown in Figure 5. It is observed from Figure 4 that the overhang section of the part tends to accumulate heat due to the insulating nature of the surrounding powder.

The temperature values predicted from simulation will be used as inputs to the machine learning model. Similar to the photodetector data, temperature readings 60 overhang section hatches and 60 bulk section hatches are recorded for the simulation. The mean and standard deviation of temperature for each block in a hatch is calculated based on the temperature at that

particular instant from 15 preceding blocks to account for the thermal history of the process. The parameters used for simulation and thermal properties of the material are reported in Table 1.

Table 1: Parameters and their corresponding values used in simulation of the test artifact.

Simulation Parameters	**Values**
Layer thickness [mm]	0.2
Hatch thickness [mm] (h_t)	0.1
Stripe length [mm] (S_L)	4
Block length [mm] (b_L)	0.4
Total number of nodes in the part	12,400
Neighborhood distance, ε [mm]	3
Gain factor	3×10^6
Thermal Properties	**Values**
Convection coefficient wall to powder, h_w [W/m^2. K]	1×10^{-6}
Convection coefficient substrate (sink), h_s [W/m^2. K]	1×10^{-2}
Thermal diffusivity (α), [m^2/s]	3.4×10^{-6}
Density, ρ [kg/m^3]	8,440
Ambient temperature, T_∞ (K)	298

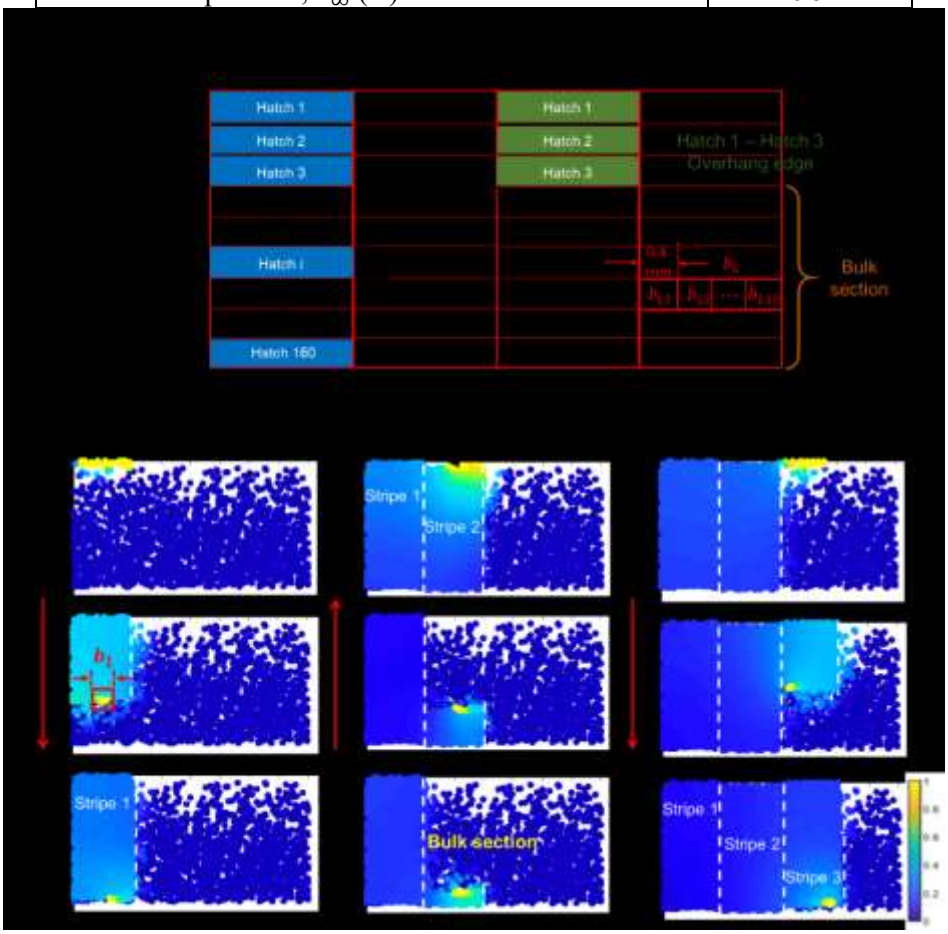

Figure 4: LPBF simulation of a layer of the overhang part done using spectral graph theory. The simulation is done stripe-wise similar to the print strategy. Heat accumulation in the overhang edge is observed.

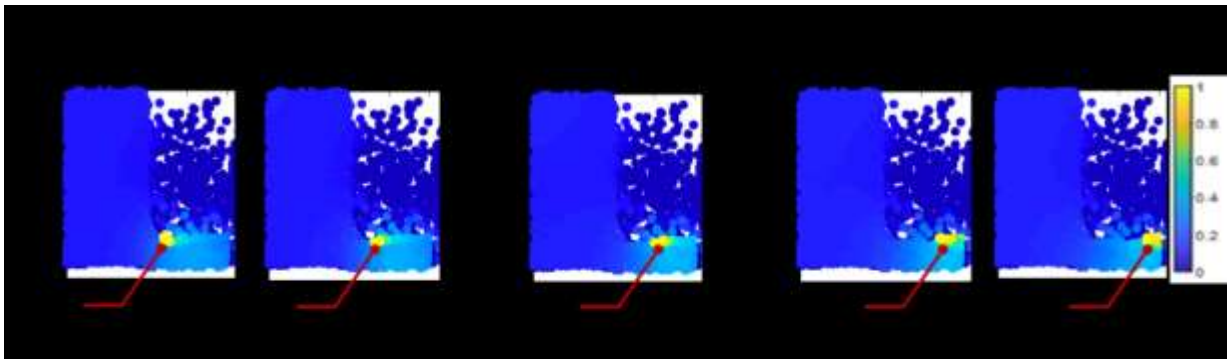

Figure 5: Block-by-block sintering of a hatch in the overhang part using a moving heat source. In this work, $N = 10$, i.e., each block is sintered with 10 blocks, and each block has 4 nodes.

4.4 Predicting the Signatures Belonging to Different Sections of the Part.

The digital twin is implemented in the following manner. The aim is to classify the difference between the overhang and bulk sections of the part shown in Figure 4 by combining data from the photodetector and thermal model. The results are cross-verified with the thermal camera, which is treated as the ground truth. This is achieved by using the mean and standard deviation of the photodetector signal within a window of ~500 μs corresponding to ~500 data points. Likewise, the mean and standard deviation of the temperature predicted by the graph theory approach are used as features representing the theoretical side of the digital twin. The features are combined in a support vector machine (SVM) model with a linear kernel.

The SVM model is chosen given its simplicity of implementation, ease of interpretation, and because it needs few hyper-parameters. The SVM model is trained and tested using the five-fold cross-validation technique. To explain further, the model is trained on 94 data points out of the 118 data points available ($4/5^{th}$ of the total data), and the remaining 24 data points ($1/5^{th}$ of the total data) are used for testing. This procedure is repeated 5-times during which the training and testing data is randomly selected, and finally, the classification accuracy is reported in the form of F-score. The F-score is a measure between 0 and 1 (larger the better) that assess both Type I (precision) and Type II prediction errors (recall) simultaneously [16].

From Table 2, it is observed that the pooling of thermal simulation and in-situ sensor data results in a classification fidelity of 87%; in contrast when the simulation and in-situ sensor data is used alone, the F-score decreases to ≈76%. The resulting confusion matrix is appended in the bottom of Table 2. To validate these results, the classification accuracy is compared against the thermal camera images of the meltpool; i.e., the high-resolution thermal camera images are considered as a baseline ground truth.

Table 2: The performance (F-score) of using the sensor data features (meltpool intensity captured by the photodetector), simulation data, and both sensor and simulation data for predicting the process condition (bulk and overhang) in the LPBF-produced overhang geometry part. The results are compared to the thermal camera data (ground truth).

Data	**Input features and Data**	**F-score**
Photodetector data	2: mean, standard deviation of intensity readings taken over 60 consecutive hatches in a moving window. Data is available for 320 total hatches.	79.6% (1.5)
Simulation data	2: mean, standard deviation of temperature predictions for 15 consecutive blocks. There are 10 blocks per hatch, for a total of 3200 simulation blocks.	76.3% (1.1)
Digital Twin Photodetector + Simulation data	2: mean, standard deviation of intensity readings + 2: mean, standard deviation of temperature readings.	87.5% (1.4)
Ground truth: Thermal camera data	2: mean, standard deviation of intensity readings.	93.2% (1.9)

Confusion Matrix for two-Level Classification (Photodetector + Simulation)		
True Classes ↓	Predicted Classes	
	Bulk	Overhang
Bulk	57 (out of 59)	2 (False Alarm)
Overhang	12 (Failing to detect)	47 (out of 59)

The F-score resulting from using the mean and standard deviation of the thermal camera images is close to 93%. However, the thermal camera costs over $300,000, viz., nearly half as much as that of an LPBF machine. Instead, the photodetector and simulation data is significantly more cost-effective (~$500) and yet the prediction fidelity achieved by the photodetector when the data acquired therefrom is combined with a physics-based thermal model is within 6% of the infrared camera. On the suggestion of one of the anonymous reviewers we also combined the

ground truth infrared thermal sensor data with theoretical simulation results, the F-score improved marginally by about 1.7 % from 93.2% to 94.9% (1.2% standard deviation).

5 Case 2 – Implementing the Digital Twin in Directed Energy Deposition

5.1 Experimental setup and data acquisition procedure

A Titanium alloy (Ti6Al4V) thin-wall test part is built on an Optomec LENS 750 DED, which as shown in Figure 6, is instrumented with sensing array which consists of a coaxial dual-wavelength pyrometer and an off-axis infrared thermal camera. The part is 55 mm × 1.78 mm × 27.5 mm (length × width × height), and is built under the following conditions: laser power 300 W, scan speed 12.7 mm/sec, and the layer thickness of 0.508 mm. It takes 50 layers and 4 hours to build the part. Further details of the sensing and experimental setup are described in Ref. [17].

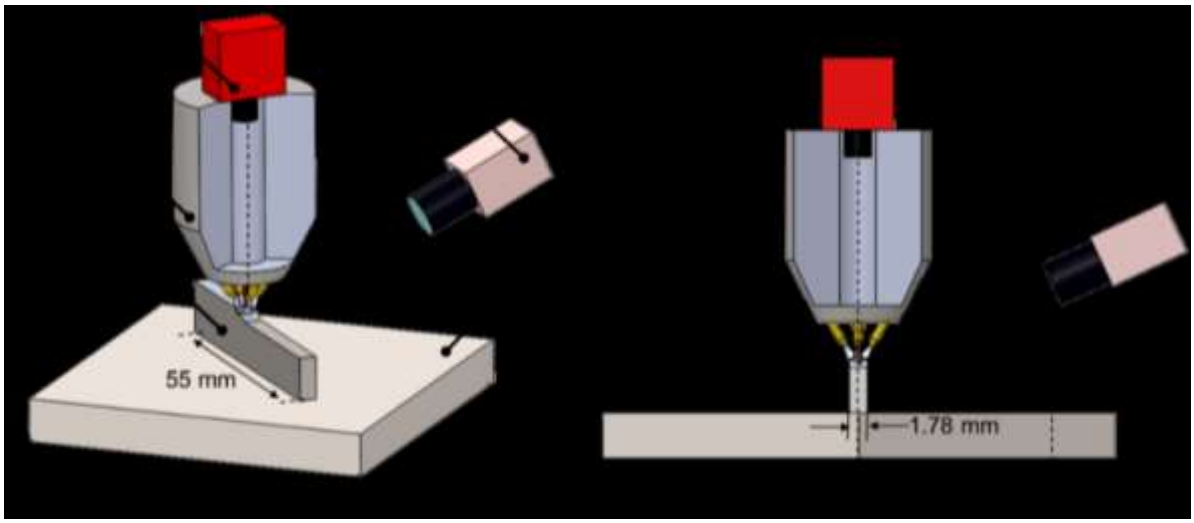

Figure 6: The sensing layout of the DED machine equipped with a pyrometer and an infrared thermal camera.

After the part is built, it is examined using X-ray computed tomography (XCT), and locations of flaws of diameter larger than 100 μm are recorded. We hypothesize that flaws occur due to accumulation of heat as the layers are deposited and the part grows in size – one of the characteristic difficulties in building thin-wall DED parts. To impede flaws due to overheating of

the part, researchers often use a lower laser power near the top layers of tall and thin-wall builds [33].

Figure 7 illustrates representative pyrometer images recorded in the regions where flaws were detected; the pyrometer signals depict a considerable difference in the shape of the meltpool for regions where flaws are absent versus those locations where flaws are present.

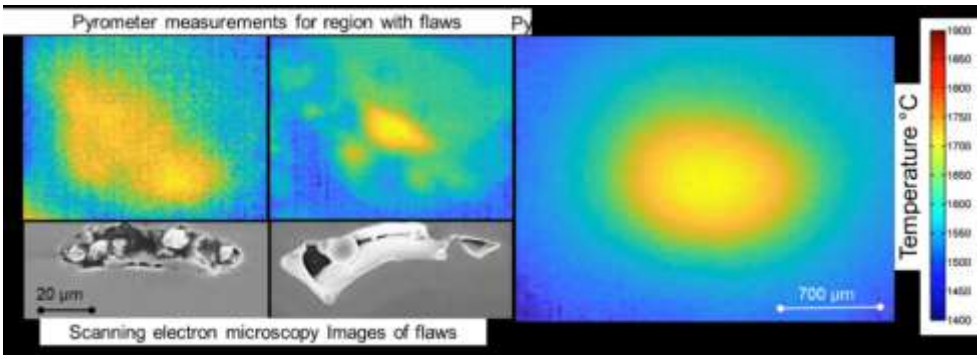

Figure 7: Pyrometer frames depicting the irregular meltpool shapes and part flaws observed during offline characterization of a region in the thin-wall. A flaw-free region, in stark contrast, depicts a uniformly shaped meltpool [17].

5.2 Thermal simulation of the thin-wall DED part.

In this work 26 pyrometer images are acquired per layer of the thin-wall. Hence, the simulation steps can be discretized per layer into 26 blocks, so that each block corresponds to a pyrometer image as shown in Figure 8. The simulation parameters for DED of the thin-wall part are given in Table 3.

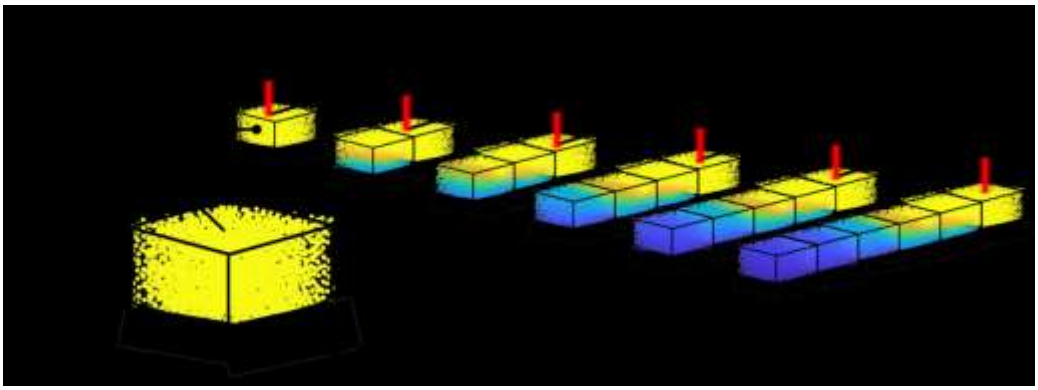

Figure 8: The discrete block-by-block heating of a hatch while simulating the DED process. A temperature gradient can be seen in the hatch by the time the simulation has reached time step t_6. Each block has an equal number of nodes inside it.

The thermal distribution of the entire part recorded at layer 7 in terms of normalized temperature from the infrared thermal camera is shown in Figure 9(a) and qualitatively at various layers in Figure 9(b). We note that these temperatures recorded by the thermal camera have been normalized between 0 and 1, because the actual part temperature, in absence of the thermal emissivity parameters, cannot be precisely ascertained. The observed thermal trends are compared with those predicted using graph theory; the mean absolute percentage error (MAPE) between simulation and the data recorded by thermal camera data is assessed to be 8%.

Table 3: The simulation parameters used for simulating the DED of the thin wall.

Simulation Parameters	Values
Layer thickness (mm)	0.508
Hatch thickness (mm)	1.78
Block length (mm)	2.1
Total number of nodes in the part	15,600
Neighborhood distance, ε (mm)	3.5
Gain factor (g)	2×10^{6}
Thermal Properties	**Values**
Convection coefficient wall, h_w (W/m^2. K)	1×10^{-6}
Convection coefficient substrate (sink), h_s (W/m^2. K)	1×10^{-2}
Thermal diffusivity, α (m^2/s)	7×10^{-6}
Density, ρ (kg/m^3)	4,300
Ambient temperature, T_∞ (K)	298

Continuing with the analysis, we further isolate the meltpool from other sections of the part, the pyrometer signatures are filtered using the threshold value of 1600 ^{o}C which is considered as the melting temperature of Ti6Al4V, as described in our previous publication [17]. In Figure 10, the temperature derived from the graph-based simulation at each layer is compared with the pyrometer data layer-by-later. The data reported at each layer is the mean of measurement from 26 blocks. The error bars in Figure 10 are representative of ± 1 standard deviation from the mean temperature for that layer (data from 26 blocks). A clearly increasing trend is evident in both the simulated and measured temperature. We note that the part-level temperature trends predicted by the graph theory approach are in normalized temperature units.

The increasing trend in part temperature with build height is to be expected in thin-wall geometries, because the increasing distance between the layer and substrate (which acts as a heat sink) impedes the conduction of heat away from the part, and hence the heat tends to accumulate near the topmost layers of the part and consequently causes material consolidation errors and flaws, such as those seen in Figure 7 [34].

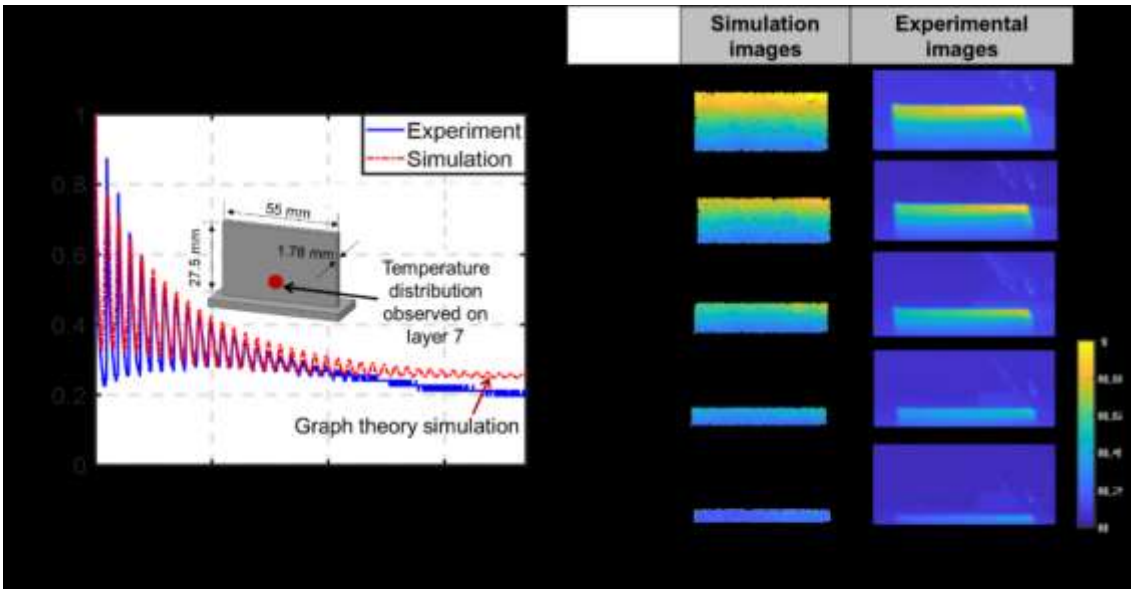

Figure 9: (a) The experimental data observed for layer 7 from the IR thermal camera are juxtaposed against the graph-theoretic simulated results. (b) The visual depiction of the heat distribution in the thin wall part observed with a thermal camera, and predicted by the graph-theoretic simulation at various layers.

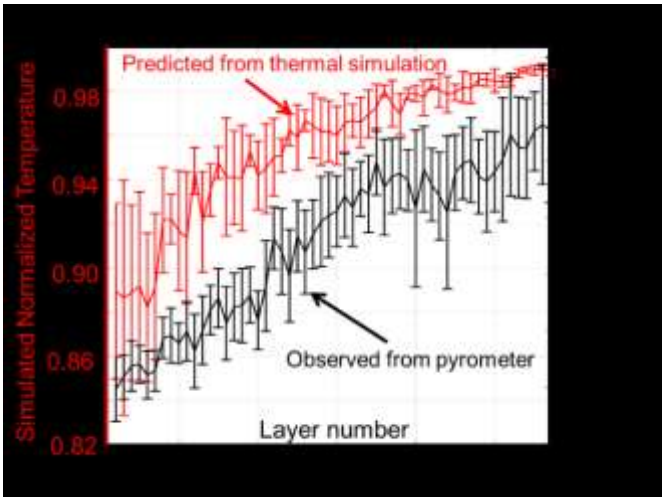

Figure 10: Comparing the trends of simulated temperature in each layer to the measured meltpool temperature from the pyrometer. The error bars are ± 1 standard deviation long.

5.3 Predicting the Occurrence of Flaws in DED-processed Thin wall Parts.

We now combine the block-by-block meltpool data in each layer recorded by the in-situ pyrometer and the corresponding graph-derived simulated temperature to detect the occurrence of flaws in a machine learning framework. As in the previous LPBF case study in Section 4, we chose the support vector machine (SVM) model, and use only four features (predictors) as inputs into the SVM to avoid overfitting of the model to the data. These four features are the mean and standard deviation of the normalized simulated temperature value for the node in each block, and the corresponding mean and standard deviation of the meltpool area, i.e., the meltpool shape characteristic. The output is a binary measure, i.e., the presence or absence of a flaw exceeding 100 μm at each simulated block. We have not used the thermal camera data because it does not encapsulate the meltpool level phenomena and the temperature recorded is not absolute.

The training data is manually labeled, in that the XCT data is stratified based on visual demarcation into two parts, namely, locations free from material consolidation flaws, and those locations where flaws are present. The flaw-afflicted locations are then grouped into the 26 blocks per layer in alignment with the pyrometer sensor measurements obtained per layer. We note that the number of flaw-free locations dominate those with flaws, in other words, the data is unbalanced. This unbalanced data set will cause the machine learning model to become unfairly biased towards prediction of flaw-free states causing high Type II errors. Further, to avoid overfitting, the data used for training and testing the SVM models are constrained to have equal number of blocks (38 blocks) that are defect-free and show porosity-related defects.

The input vectors used for training the SVM consists of 61 out of a total of 76 blocks, and 15 for testing. A five-fold cross-validation procedure is enforced, and the representative confusion matrix from this classification study is reported in Table 4; the F-score metric is ≈ 91% with a standard deviation of 1.2% over replications.

In comparison, as shown in Table 4, when only data from the simulation or sensor data is used, the F-score is in the range of 80% to 83%. The confusion matrix with the pyrometer and simulation data are reported in the bottom of Table 4. One also notes the decrease in prediction uncertainty resulting from the digital twin model.

Table 4: The performance (F-score) of using the sensor data (meltpool area features from the pyrometer), simulation data, and both sensor and simulation data for predicting the occurrence of flaws in the DED-produced thin-wall part.

Data	**Input features**	**F-Score**
Pyrometer data	2: mean, standard deviation of meltpool area.	81.6% (3.2%)
Simulation data	2: mean, standard deviation of temperature readings.	82.9% (2.7%)
Digital Twin Pyrometer + Simulation data	2: mean, standard deviation of pyrometer readings. + 2: mean, standard deviation of temperature readings.	91.0% (1.2%)
Confusion Matrix for two-level classification (Pyrometer + Simulation)		
True Classes ↓	Predicted Classes	
	Flaw-free	Flaws
Flaw-free (38 total)	38	0 (False Alarm, Type I error)
Flaws (38 total)	6 (Failing to detect, Type II error)	32

The improvement in the prediction fidelity from 80% to 90% is important from a quality assurance perspective in AM [1]. The results reinforce the central message of this paper that pooling in-situ sensor measurements and predictions from a physical model results in more accurate prediction of defects compared to using either experimental data or simulation alone.

Moreover, we used a very rudimentary machine learning approach, namely SVM, as opposed to relatively hyper-parameter intensive and computation-intensive techniques such as self-organizing maps and deep learning neural networks to realize this aim [17, 24, 25]. Pertinently, the computational burden in storage and analysis of data is mitigated significantly using the digital twin approach as only the first two statistical moments (mean and standard deviation) from the sensor signatures need to be extracted.

6 Conclusions and Future Work

This work demonstrates the concept of the digital twin in additive manufacturing (AM). The key idea is to combine physics-driven predictions with in-situ sensor data and machine learning to detect potential anomalies in the AM process. Specifically, this work shows that by augmenting the insight into the process physics gained through a theoretical model with real-time information from in-situ sensor data in a machine learning framework leads to higher statistical fidelity of detecting process flaws, compared to using only the theoretical model-derived predictions or in-situ sensor data alone.

The effectiveness of the digital twin approach proposed in this work was substantiated with experimental data obtained for the laser powder bed fusion (LPBF) and directed energy deposition (DED) metal AM processes as follows:

(1) A novel graph theory-based approach is used to predict the instantaneous spatiotemporal temperature distribution in the LPBF and DED parts. This approach is considerably more computationally efficient than finite element models used in AM research while maintaining similar prediction accuracy [7].

(2) In the LPBF process, an Inconel 625 part with an overhang feature was printed. While overhang features are not defects, they are challenging to build and often fail due to heat accumulation. Hence it is important to predict the impending failure of overhang features. The thermal distribution in the part was predicted using the graph-theoretic computational heat transfer model. By combining the part-level thermal history predicted by the graph theory model with in-situ meltpool intensity observations acquired using a photodetector, the process condition, i.e., whether a bulk or overhang feature is being printed is identified with accuracy

close to 88%. The prediction fidelity compares favorably with the ground truth data acquired from a meltpool thermal camera (≈ 92%).

(3) A further important result from the LPBF case is that the digital twin considerably improves the prediction fidelity of a relatively inexpensive photodetector sensor (which costs less than $500), to the level of a much more expensive meltpool thermal camera costing over $300,000.

(4) For the DED-related case, we use the graph theory approach to predict the temperature distribution in a thin-wall titanium alloy part, and subsequently, combined these predictions with meltpool temperature data acquired from a two-color, coaxial in-situ pyrometer. The statistical fidelity (F-score) in predicting locations with flaws is close to 80% when only either the thermal model or the meltpool sensor data is used without the other. However, when used together, the prediction fidelity improves to 90% - a significant improvement in the context of the AM field.

(5) In both the DED and LPBF cases, rudimentary features, namely, mean and standard deviation were extracted from the sensor data and used as inputs for prediction of flaws. Accordingly, the digital twin approach considerably reduces the computational burden involved in the storage of raw sensor data and subsequent calculation of several dozen signal features that is typically required in complex data-driven machine learning methods.

In our future work, we will further substantiate the concept of the digital twin in the context of the prediction of different types of flaws, such as cracking and deformation, with data acquired from multiple in-situ sensors.

Acknowledgments

The data for the laser powder bed fusion case study described in Sec. 4 was acquired by Dr. Brandon Lane at the National Institute of Standards and Technology; the authors duly acknowledge his willingness to share the data. The authors thank the three anonymous reviewers whose constructive comments and suggestions have doubtlessly improved the rigor of this work. The authors also thank the Associate Editor of the Transactions, Professor Zhenyu Kong for shepherding this work through the review process.

Funding

Prahalada Rao thanks the National Science Foundation for funding his research through the following grants CMMI-1719388, CMMI-1739696 and CMMI-1752069 (CAREER). Specifically, the concept of combining modeling, sensing, and analytics to detect incipient faults towards a correct-as-you-build smart additive manufacturing paradigm was funded through CMMI-1752069. The foregoing NSF CAREER grant has provided additional supplemental funding towards internships for the two student co-authors via the NSF INTERN program; Mr. Reza Yavari and Mr. Aniruddha Gaikwad are currently interning at Edison Welding Institute (Ohio) and Lawrence Livermore National Laboratories, respectively.

References Cited

[1] Huang, Y., Leu, M. C., Mazumder, J., and Donmez, A., 2015, "Additive Manufacturing: Current State, Future Potential, Gaps and Needs, and Recommendations," Journal of Manufacturing Science and Engineering, 137(1), pp. 014001-014001-014010.doi:10.1115/1.4028725

[2] Kellner, T., 2018, "Fired Up: GE Successfully Tested Its Advanced Turboprop Engine With 3D-Printed Parts," GE reports.

[3] Sames, W. J., List, F., Pannala, S., Dehoff, R. R., and Babu, S. S., 2016, "The metallurgy and processing science of metal additive manufacturing," International Materials Reviews, 61(5), pp. 315-360

[4] Taheri, H., Shoaib, M. M., Koester, L. W., Bigelow, T. A., Collins, P. C., and Bond, L. J., 2017, "Powder based additive manufacturing-A review of types of defects, generation mechanisms, detection, property evaluation and metrology," Int. J. Addit. Subtractive Mater. Manuf, 1(2), pp. 172-209

[5] DebRoy, T., Wei, H., Zuback, J., Mukherjee, T., Elmer, J., Milewski, J., Beese, A., Wilson-Heid, A., De, A., and Zhang, W., 2018, "Additive manufacturing of metallic components–process, structure and properties," Progress in Materials Science, 92, pp. 112-224

[6] Karayagiz, K., Elwany, A., Tapia, G., Franco, B., Johnson, L., Ma, J., Karaman, I., and Arróyave, R., 2019, "Numerical and experimental analysis of heat distribution in the laser powder bed fusion of Ti-6Al-4V," IISE Transactions, 51(2), pp. 136-152.doi:10.1080/24725854.2018.1461964

[7] Yavari, M. R., Cole, K. D., and Rao, P., 2019, "Thermal Modeling in Metal Additive Manufacturing using Graph Theory," Journal of Manufacturing Science and Engineering, 141(7), pp. 071007-071026

[8] Knapp, G., Mukherjee, T., Zuback, J., Wei, H., Palmer, T., De, A., and DebRoy, T., 2017, "Building blocks for a digital twin of additive manufacturing," Acta Materialia, 135, pp. 390-399

[9] DebRoy, T., Zhang, W., Turner, J., and Babu, S. S., 2017, "Building digital twins of 3D printing machines," Scripta Materialia, 135, pp. 119-124.doi:https://doi.org/10.1016/j.scriptamat.2016.12.005

[10] Mukherjee, T., and DebRoy, T., 2019, "A digital twin for rapid qualification of 3D printed metallic components," Applied Materials Today, 14, pp. 59-65

[11] Yang, Z., Eddy, D., Krishnamurty, S., Grosse, I., Denno, P., Lu, Y., and Witherell, P., 2017, "Investigating Grey-Box Modeling for Predictive Analytics in Smart Manufacturing," ASME, International Design Engineering Technical Conferences and Computers and Information in Engineering Conference Cleaveland, OH, pp. V02BT03A024-034.

[12] Yang, Z., 2018, "Model-based Predictive Analytics for Additive and Smart Manufacturing," Ph.D. Dissertation, University of Massachusetts, Amherst.

[13] Bandyopadhyay, A., and Traxel, K. D., 2018, "Invited Review Article: Metal-additive manufacturing—Modeling strategies for application-optimized designs," Additive Manufacturing

[14] Francois, M. M., Sun, A., King, W. E., Henson, N. J., Tourret, D., Bronkhorst, C. A., Carlson, N. N., Newman, C. K., Haut, T., Bakosi, J., Gibbs, J. W., Livescu, V., Vander Wiel, S. A., Clarke, A. J., Schraad, M. W., Blacker, T., Lim, H., Rodgers, T., Owen, S., Abdeljawad, F., Madison, J., Anderson, A. T., Fattebert, J. L., Ferencz, R. M., Hodge, N. E., Khairallah, S. A., and Walton, O.,

2017, "Modeling of additive manufacturing processes for metals: Challenges and opportunities," Current Opinion in Solid State and Materials Science, 21(4), pp. 198-206.doi:https://doi.org/10.1016/j.cossms.2016.12.001

[15] Luo, Z., and Zhao, Y., 2018, "A survey of finite element analysis of temperature and thermal stress fields in powder bed fusion Additive Manufacturing," Additive Manufacturing, 21, pp. 318-332.doi:https://doi.org/10.1016/j.addma.2018.03.022

[16] Montazeri, M., and Rao, P., 2018, "Sensor-Based Build Condition Monitoring in Laser Powder Bed Fusion Additive Manufacturing Process Using a Spectral Graph Theoretic Approach," Journal of Manufacturing Science and Engineering, 140(9), p. 091002

[17] Khanzadeh, M., Chowdhury, S., Tschopp, M. A., Doude, H. R., Marufuzzaman, M., and Bian, L., 2019, "In-situ monitoring of melt pool images for porosity prediction in directed energy deposition processes," IISE Transactions, 51(5), pp. 437-455.doi:10.1080/24725854.2017.1417656

[18] Khairallah, S. A., Anderson, A. T., Rubenchik, A., and King, W. E., 2016, "Laser powder-bed fusion additive manufacturing: Physics of complex melt flow and formation mechanisms of pores, spatter, and denudation zones," Acta Materialia, 108, pp. 36-45

[19] King, W., Anderson, A., Ferencz, R., Hodge, N., Kamath, C., and Khairallah, S., 2014, "Overview of modelling and simulation of metal powder-bed fusion process at Lawrence Livermore National Laboratory," Materials Science and Technology, 31(8), pp. 957-968

[20] Seifi, M., Salem, A., Beuth, J., Harrysson, O., and Lewandowski, J. J., 2016, "Overview of Materials Qualification Needs for Metal Additive Manufacturing," JOM, 68(3), pp. 747-764.doi:10.1007/s11837-015-1810-0

[21] Grasso, M., and Colosimo, B. M., 2017, "Process defects and in situ monitoring methods in metal powder bed fusion: a review," Measurement Science and Technology, 28(4), p. 044005

[22] Mani, M., Lane, B. M., Donmez, M. A., Feng, S. C., and Moylan, S. P., 2017, "A review on measurement science needs for real-time control of additive manufacturing metal powder bed fusion processes," International Journal of Production Research, 55(5), pp. 1400-1418

[23] Imani, F., Gaikwad, A., Montazeri, M., Rao, P., Yang, H., and Reutzel, E., 2018, "Process Mapping and In-Process Monitoring of Porosity in Laser Powder Bed Fusion Using Layerwise Optical Imaging," Journal of Manufacturing Science and Engineering, 140(10), pp. 101009-101009-101014.doi:10.1115/1.4040615

[24] Williams, J., Dryburgh, P., Clare, A., Rao, P., and Samal, A., 2018, "Defect Detection and Monitoring in Metal Additive Manufactured Parts through Deep Learning of Spatially Resolved Acoustic Spectroscopy Signals," Smart and Sustainable Manufacturing Systems, 2(1), pp. 204-226.doi:10.1520/SSMS20180035

[25] Yuan, B., Guss, G. M., Wilson, A. C., Hau-Riege, S. P., DePond, P. J., McMains, S., Matthews, M. J., and Giera, B., 2018, "Machine-Learning-Based Monitoring of Laser Powder Bed Fusion," Advanced Materials Technologies, 3(12), p. 1800136.doi:10.1002/admt.201800136

[26] Scime, L., and Beuth, J., 2018, "A multi-scale convolutional neural network for autonomous anomaly detection and classification in a laser powder bed fusion additive manufacturing process," Additive Manufacturing, 24, pp. 273-286

[27] Gouge, M., and Michaleris, P., 2018, Thermo-Mechanical Modeling of Additive Manufacturing, Elsevier, Cambridge, MA.

[28] Seifi, S. H., Tian, W., Doude, H., Tschopp, M. A., and Bian, L., 2019, "Layer-wise modeling and anomaly detection for laser-based additive manufacturing," Journal of Manufacturing Science and Engineering, 141(8), pp. 081013-081025

[29] Fox, J. C., Moylan, S. P., and Lane, B. M., 2016, "Effect of process parameters on the surface roughness of overhanging structures in laser powder bed fusion additive manufacturing," Procedia CIRP, 45, pp. 131-134

[30] Cheng, B., and Chou, K., 2015, "Geometric consideration of support structures in part overhang fabrications by electron beam additive manufacturing," Computer-Aided Design, 69, pp. 102-111.doi:https://doi.org/10.1016/j.cad.2015.06.007

[31] Atzeni, E., and Salmi, A., 2015, "Study on unsupported overhangs of AlSi10Mg parts processed by Direct Metal Laser Sintering (DMLS)," Journal of Manufacturing Processes, 20, pp. 500-506.doi:10.1016/j.jmapro.2015.04.004

[32] Cheng, B., and Chou, K., 2015, "Deformation Evaluation of Part Overhang Configurations in Electron Beam Additive Manufacturing," ASME 2015 International Manufacturing Science and Engineering Conference, pp. V001T002A072-V001T002A072

[33] Johnson, K. L., Rodgers, T. M., Underwood, O. D., Madison, J. D., Ford, K. R., Whetten, S. R., Dagel, D. J., and Bishop, J. E., 2018, "Simulation and experimental comparison of the thermo-mechanical history and 3D microstructure evolution of 304L stainless steel tubes manufactured using LENS," Computational Mechanics, 61(5), pp. 559-574

[34] Peyre, P., Aubry, P., Fabbro, R., Neveu, R., and Longuet, A., 2008, "Analytical and numerical modelling of the direct metal deposition laser process," Journal of Physics D: Applied Physics, 41(2), p. 025403